



Philosophical Magazine Letters

ISSN: 0950-0839 (Print) 1362-3036 (Online) Journal homepage: www.tandfonline.com/journals/tphl20

***In-situ* S/TEM investigations of deformation and damage mechanisms in neutron-irradiated EUROFER97**

Qian Yuan, Ankur Chauhan, Lakshay Chauhan, Dimitri Litvinov, Ermile Gaganidze, Hans-Christian Schneider & Jarir Aktaa

To cite this article: Qian Yuan, Ankur Chauhan, Lakshay Chauhan, Dimitri Litvinov, Ermile Gaganidze, Hans-Christian Schneider & Jarir Aktaa (2025) *In-situ* S/TEM investigations of deformation and damage mechanisms in neutron-irradiated EUROFER97, Philosophical Magazine Letters, 105:1, 2512307, DOI: [10.1080/09500839.2025.2512307](https://doi.org/10.1080/09500839.2025.2512307)

To link to this article: <https://doi.org/10.1080/09500839.2025.2512307>



© 2025 Karlsruhe Institute of Technology.
Published by Informa UK Limited, trading as
Taylor & Francis Group



Published online: 03 Jun 2025.



Submit your article to this journal [↗](#)



Article views: 326



View related articles [↗](#)



View Crossmark data [↗](#)

In-situ S/TEM investigations of deformation and damage mechanisms in neutron-irradiated EUROFER97

Qian Yuan^a, Ankur Chauhan^{a,b}, Lakshay Chauhan^a, Dimitri Litvinov^a,
Ermile Gaganidze^a, Hans-Christian Schneider^a and Jarir Aktaa^a

^aKarlsruhe Institute of Technology (KIT), Institute for Applied Materials, Eggenstein-Leopoldshafen, Germany; ^bExtreme Environments Materials Group (EEMG), Department of Materials Engineering, Indian Institute of Science, Bengaluru, India

ABSTRACT

In this work, we employed *in-situ* S/TEM techniques to investigate deformation and damage mechanisms in neutron-irradiated reduced-activation ferritic/martensitic (RAFM) EUROFER97 steel subjected to a dose of 15 dpa at 330 °C. The irradiated microstructure revealed uniformly distributed dislocation loops and sporadic nanometer-sized cavities. During *in-situ* straining of a focused-ion beam (FIB)-prepared lamella, mobile line dislocations were observed to interact with dislocation loops, leading to loop absorption and the formation of dislocation networks. Further straining resulted in the formation of a dislocation-loop-free zone. Within this region, deformation-induced nanometer-sized cavities emerged, likely from pre-existing irradiation-induced clusters, cavities, or remnants of absorbed loops. Coalescence of these cavities led to the formation of micro-cracks and ultimately to the fracture of the lamella. This suggests premature failure of the irradiated sample compared to its unirradiated counterpart, highlighting irradiation-induced embrittlement.

ARTICLE HISTORY



Received 10 June 2024
Accepted 23 May 2025

KEYWORDS

In-situ S/TEM straining; deformation and damage mechanisms; neutron irradiation; irradiation-induced defects; RAFM steel

1. Introduction

The mechanical properties of structural materials intended for use in upcoming nuclear fusion reactors are known to degrade under extreme working conditions, such as high-dose of neutron irradiation (greater than 14 MeV) at elevated temperatures [1–6]. RAFM-steels are currently considered the most promising candidate for the first wall of nuclear fusion reactors and have undergone extensive studies [7,8]. The reason for this consideration is primarily attributed to two main factors. Compared to austenitic stainless steels, RAFM steels exhibit excellent resistance against irradiation-induced swelling and high-temperature helium embrittlement [8,9]. Additionally, the alloying elements in RAFM

CONTACT Qian Yuan ✉ qian.yuan@partner.kit.edu  Karlsruhe Institute of Technology (KIT), Institute for Applied Materials, Hermann-von-Helmholtz-Platz 1, Eggenstein-Leopoldshafen 76344, Germany; Ankur Chauhan ✉ ankurchauhan@iisc.ac.in  Karlsruhe Institute of Technology (KIT), Institute for Applied Materials, Hermann-von-Helmholtz-Platz 1, Eggenstein-Leopoldshafen 76344, Germany and now at Extreme Environments Materials Group (EEMG), Department of Materials Engineering, Indian Institute of Science, Bengaluru 560012, Karnataka, India

© 2025 Karlsruhe Institute of Technology. Published by Informa UK Limited, trading as Taylor & Francis Group
This is an Open Access article distributed under the terms of the Creative Commons Attribution License (<http://creativecommons.org/licenses/by/4.0/>), which permits unrestricted use, distribution, and reproduction in any medium, provided the original work is properly cited.

steels are carefully selected to minimise the presence of highly radioactive and volatile nuclides, ensuring fast decay of radioactive isotopes below the recycling limit. Despite these advantages, RAFM steels typically experience low-temperature irradiation hardening accompanied by loss of ductility and embrittlement based on the level of neutron irradiation, posing challenges to their potential use in future fusion reactors [2,10].

The degradation of mechanical properties is primarily ascribed to microstructural defects induced by irradiation, including dislocation loops, cavities, solute clustering, precipitates, and grain boundary segregation [1–5]. Dislocation loops, in particular, are recognised as the main contributors to the irradiation hardening of RAFM steels at low-irradiation temperatures [3]. They act as obstacles for line dislocations during plastic deformation. To predict the yield strength, hardening models such as dispersed barrier hardening (DBH) or Friedel Kroupa Hirsch (FKH) models are utilised [11–13]. These hardening models establish a correlation between the density and size of the irradiation-induced defects (i.e. dislocation loops, cavities, and precipitates) with the resulting increase in yield strength [12,14]. However, these statistical approaches do not offer insights into the deformation mechanisms. For example, two $\frac{1}{2}\langle 111 \rangle$ type dislocation loops can either annihilate during plastic deformation when having opposite Burgers vectors (e.g. $\frac{1}{2}[111]$ and $\frac{1}{2}[\bar{1}\bar{1}\bar{1}]$) or transform into a $\langle 100 \rangle$ type loop through a shear reaction (e.g. $\frac{1}{2}[111] + \frac{1}{2}[1\bar{1}\bar{1}] = [100]$). However, such evolution is not captured in the hardening model; instead, the DBH model treats the two $\frac{1}{2}\langle 111 \rangle$ type loops as individual loops, increasing yield strength in both scenarios. Additionally, deformation localisation (sometimes referred to as channelling) is recognised as a primary deformation mechanism in irradiated materials [33,34]. However, due to the experimental challenges, the dynamic behaviour of irradiation-induced defects under applied strain is scarcely studied in RAFM steels. Experimentally, *in-situ* TEM straining makes direct observation of dislocation loop and line dislocation interaction possible [15–17]. For instance, in ion-irradiated Fe–Cr alloys, the Burgers vector of dislocation loops can be altered from $\langle 100 \rangle$ to $\frac{1}{2}\langle 111 \rangle$ during the *in-situ* straining [17].

This study addresses the identified research gap by examining the evolution of irradiation-induced defects in RAFM EUROFER97 steel under applied strain using *in-situ* S/TEM techniques. EUROFER97 steel is chosen due to its distinctive defect characteristics, featuring a high density of uniformly distributed dislocation loops after neutron irradiation [18,19]. Moreover, the line dislocation density remains notably high, approximately 10^{14} m^{-2} , even in the unirradiated case [20,21]. Therefore, in this study, the substantially high density of dislocation loops and pre-existing line dislocations offers the opportunity to directly observe their interaction in STEM mode, revealing the underlying deformation mechanism. Additionally, once the crack initiates, the deformation localised region presents a high density of nanometer-sized cavities that differ from the pre-existing radiation-induced cavities. The *in-situ* observation of cavity evolution in TEM mode elucidates the damage mechanism. Overall, this study provides direct evidence of the microstructural evolution upon straining as-irradiated RAFM steel.

2. Experimental details

The EUROFER97 steel, with a nominal composition of Fe–9Cr–1.1W–0.2V–0.12Ta, was produced by Boehler Austria GmbH with a heat number 83697. For further details on the

steel's manufacturing process and chemical composition, refer to [1]. The final heat treatment before irradiation included austenitization at 980°C for 30 minutes, then tempering at 760°C for 1.5 hours.

The irradiation experiments were conducted on EUROFER97 Charpy impact samples in the BOR-60 fast reactor in the Russian Federation as part of the international project 'Wissenschaftlich-Technische Zusammenarbeit 01/577' (WTZ) [22]. The samples were neutron-irradiated to a dose of 15 dpa at a temperature of 330°C [18,19]. This study utilised the Ga⁺ FEI Scios FIB scanning electron microscope (SEM) for fabricating electron-transparent lamellae. This choice offers several advantages over using 3 mm disc-shaped samples prepared via electro-polishing, including: (1) Achieving an optimised uniform thickness of the sample suitable for *in-situ* tensile straining. (2) Mitigating the impact of sample magnetism during TEM investigations. (3) Minimising radioactivity exposure.

Initially, TEM lamellae were in situ lifted out from previously electrochemically polished irradiated samples and welded onto a copper tensile grid (see Figure 1a,c). For further details on the electro-polishing technique used for sample preparation, refer to Ref. [5]. During the welding process, Pt deposition was performed using ion-assisted deposition on both sides, resulting in a total of four welding points. Each weld took about 2 minutes to complete using the double-frame overlapping/parallel welding technique in the FIB. This method was chosen to improve the mechanical stability of the welded region, ensuring it could withstand subsequent tensile loading without premature fracture. After welding, the lamella was carefully thinned from both sides by progressively reducing the beam energy from 30 kV to 5 kV. Finally, low-kV Ga⁺ ion milling (2 kV) was employed to minimise FIB-induced damage, with specific parameters for the cleaning pattern procedure outlined in Ref. [23]. The lamella thickness was measured using electron energy loss spectroscopy (EELS) integrated into the TEM microscope equipped with a post-column GIF Tridiem energy filter. Notably, thin lamellae, typically ranging from 50 to 100 nm, were specifically selected for *in-situ* TEM experiments, whereas thicker lamellae (~150 nm) were used for *in-situ* STEM investigations (Figure 1d).

In-situ TEM straining experiments were conducted using a Gatan single-tilt straining holder (see Figure 1b) in a high-resolution FEI Tecnai G2 F20 X-TWIN microscope operating at 200 kV. An accutroller control unit was employed to apply a constant elongation rate of approximately 1 µm/s. The real-time microstructure evolution under applied strain was recorded using the Gatan RioTM CMOS camera, and the acquired data were processed and analyzed with the Gatan digital micrograph software, including the *in-situ* player/editor module. Although special care was taken to maintain consistent imaging conditions throughout the *in-situ* S/TEM experiments, minor variations in defect contrast may still arise due to subtle changes in the local diffraction conditions induced by straining. Additionally, regions with distinct features, such as grain boundaries and line dislocations, were chosen as reference points, and the imaging conditions within the Region of Interest (ROI) were carefully monitored to compensate for any sample drift occurring during straining. Furthermore, given the advantages of STEM over conventional bright-field TEM for thick specimens [24], *in-situ* STEM equipped with an HAADF detector was employed in this study to observe microstructural evolution in thick TEM lamellae (~150 nm), enhancing the visibility of loops and line dislocations. However, obtaining high-quality STEM micrographs typically requires more

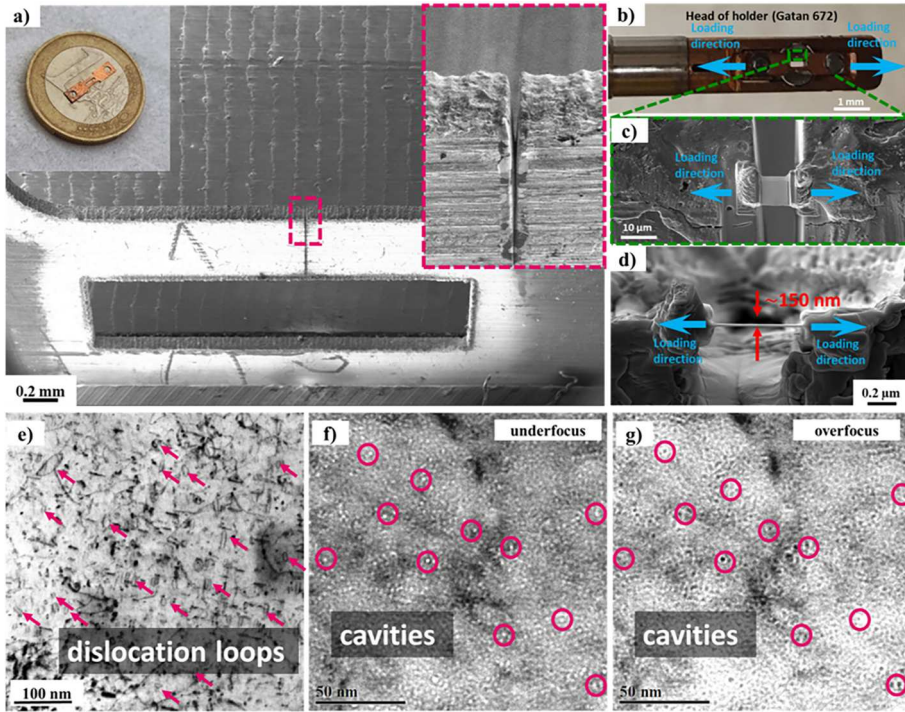


Figure 1. (a) SEM micrograph shows a gauge section of the copper tensile grid fabricated via laser cutting. The tensile grid had a total length of 11.5 mm and a thickness of 0.3 mm. The inset in the upper left corner shows the Cu grid placed on a 1 Euro coin. Additionally, the inset in the upper right corner of the micrograph showcases a notch precisely cut at the midpoint of the copper tensile grid via focused-ion beam (FIB) processing, followed by meticulous surface polishing accomplished through FIB CCS (clean cross-section) procedures. (b) The copper tensile grid is securely clamped onto the single-tilt holder with two HexlokTM (threaded fasteners with a washer head), ensuring stability. (c) and (d) illustrate the front – and top-view perspectives of the lamella affixed to the copper tensile grid through Pt welding across the notch mentioned above. (e–g) Representative microstructure of an EUROFER97 steel after neutron-irradiation to 15 dpa at 330 °C. Inverted-contrast STEM-HAADF micrograph (e) shows the homogenous distribution of dislocation loops and line dislocations. (f) and (g) present representative bright field (BF)-TEM micrographs showcasing irradiation-induced cavities rich areas. The contrast of the cavities changed from a white dot with a black Fresnel fringe in an under-focused (–1 μm) micrograph (f) to a dark dot with a white Fresnel fringe in the over-focused (+1 μm) micrograph (g).

time than conventional TEM. Consequently, a balanced frame rate of 2 fps was adopted for recording sequential STEM micrographs.

3. Results and discussion

3.1. As-irradiated microstructure

As illustrated in Figure 1e, the irradiated microstructure manifests a homogeneous distribution of the dark-contrast dislocation loops. Our previous quantitative analysis revealed a total visible loop density of about $12.1 \times 10^{21} \text{ m}^{-3}$ in an irradiated state, having a mean size of 7 nm [18]. Loop's Burgers vector determination by analyzing

weak-beam dark-field (WBDF) micrographs acquired under two-beam conditions revealed a higher fraction of $\langle 100 \rangle$ type loops in comparison to the $\frac{1}{2}\langle 111 \rangle$ variants [18,21]. Furthermore, smaller loops are predominantly of the $\frac{1}{2}\langle 111 \rangle$ type, while larger ones are mainly of the $\langle 100 \rangle$ type. The interstitial nature of the dislocation loop was determined and confirmed using the inside-outside contrast technique [25].

In addition to the dislocation loops, nanometer-sized irradiation-induced cavities were also observed. The cavity density was approximately an order of magnitude lower than the dislocation loops, measured at $3.0 \times 10^{21} \text{ m}^{-3}$ [18,26,27]. Figure 1f, g depict these nanometer-sized cavities within a region of their abundance. These micrographs were captured using the TEM bright-field through-focal series technique. Furthermore, besides dislocation loops and cavities, an appreciable density of line dislocations, elemental clusters, and segregation along loops as well as boundaries were also observed, see Ref. [20]. A summary of the quantitative data on irradiation-induced defects and pre-existing precipitates in the as-irradiated condition is presented in Table 1.

3.2. In-situ straining of the as-irradiated EUROFER97 lamella at room temperature

The sequential microstructural evolution of irradiated EUROFER97 under tensile straining is captured in Figure 2a–d through inverted-contrast STEM-HAADF micrographs, which delineate four key stages – from the onset of deformation to final fracture of the FIB-fabricated lamella. The estimated strain values corresponding to these stages are 0.1% (Stage I), 0.5% (Stage II), 3.5% (Stage III), and 26.3% (Stage IV), illustrating the progressive elongation and failure of the lamella. Although the in-situ straining was conducted under strain-rate control without direct force measurement, the expected engineering stress levels were approximated using the known tensile properties of irradiated EUROFER97 at room temperature (yield strength of $\sim 1100 \text{ MPa}$ at 0.2% strain) [35]. Given the lamella’s dimensions and the limited strain-hardening behaviour typical of irradiated materials, the estimated stress magnitudes were $\sim 200\text{--}300 \text{ MPa}$ for Stage I, $\sim 1100 \text{ MPa}$ at Stage II, $\sim 900\text{--}950 \text{ MPa}$ for Stage III, and $\sim 500\text{--}600 \text{ MPa}$ at failure in the Stage IV. These estimates provide a contextual framework for interpreting the defect evolution and microstructural changes observed during straining, as detailed in Figure 2.

At Stage I (Figure 2a), the microstructure is dominated by the motion of isolated line dislocations and their interactions with existing dislocation loops, as highlighted in the high-magnification image (see Figure 2e). With continued straining, Stage II (Figure 2b) reveals a more pronounced interaction between mobile dislocations and

Table 1. Summary of quantitative data on irradiation-induced defects and precipitates in the as-irradiated condition.

Microstructural feature	Density ($\times 10^{21} \text{ m}^{-3}$)	Mean diameter (nm)	Reference
Dislocation loops	12.1 ± 0.7	7.0	[18]
Cavities	3.0 ± 0.7	2.1	[18]
M_{23}C_6 precipitates	0.04	98	[20]
MX precipitates	0.06	28	[20]

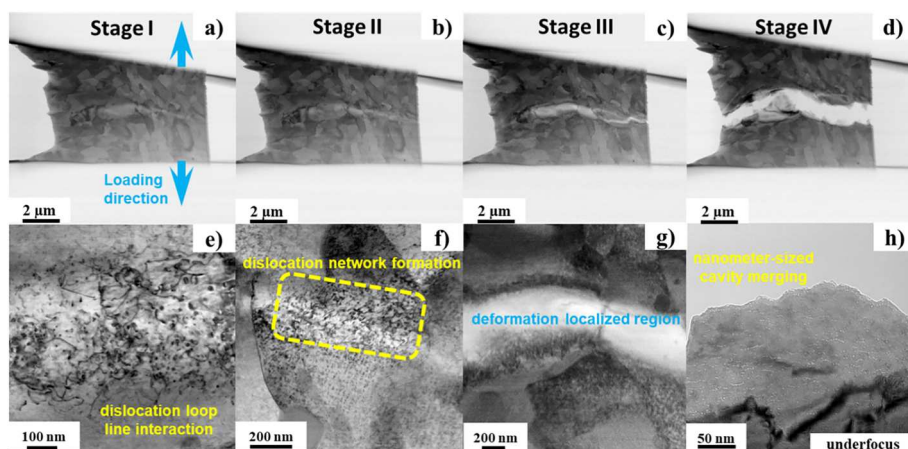


Figure 2. (a-d) Sequential inverted-contrast STEM-HAADF micrographs illustrate four distinct stages of microstructural evolution upon straining irradiated EUROFER97 lamella at room temperature. Representative inverted-contrast STEM-HAADF micrographs (e-g) and BF-TEM micrograph (h) with under-focused contrast show typical microstructure at each stage. (e) Line dislocation-loop interaction corresponds to stage I (a). (f) Line dislocations impeded by loops and the formation of the dislocation networks correspond to stage II (b). (g) Formation of a localised deformation region free of irradiation-induced dislocation loops and dislocation networks corresponds to stage III (c). (h) The merging of nanometer-sized cavities and the final failure of the lamella correspond to stage IV (d).

irradiation-induced loops, resulting in the development of complex dislocation networks and partial loop absorption (Figure 2f). This will be discussed in more detail later. As deformation progresses, it becomes highly localised in the central region of the lamella, marking Stage III (see Figure 2c). At high magnification (see Figure 2g), the deformation-localised region in light contrast shows a characteristic absence of dislocation loops in the localised area, resembling dislocation channelling frequently observed in deformed irradiated microstructures [28,29,33,34]. This suggests that the loops were either annihilated or absorbed by the gliding line dislocations during deformation. Finally, at Stage IV (Figure 2d), the accumulation of plastic strain leads to the formation and propagation of a critical crack through the deformation-localised zone, culminating in lamella failure. High-magnification observation (Figure 2h) near the fractured lamella edge reveals the presence of nanometer-scale cavities and their coalescence resulting in the final failure of the lamella. The subsequent sections provide a more detailed discussion of these evolving deformation and fracture processes.

Sequential inverted-contrast STEM-HAADF micrographs and corresponding schematics in Figure 3 highlight the dynamic behaviour of three marked dislocation loops under tensile straining. To monitor the evolution of dislocation loops under consistent diffraction conditions, loops located near grain boundaries were chosen for analysis. Overall, all three loops disappeared under the direct or indirect influence of neighbouring dislocation activities. For instance, a line dislocation, originating from the source within the grain boundary, interacts with and absorbs the marked dislocation loop 3 (refer to Figure 3f, g, h). On the contrary, the marked smaller dislocation loop 2 (in Figure 3a, f) appears to be absorbed by the larger loop 1 (in Figure 3c, h). This evolution seems to occur without the loops' direct interaction with the line dislocations. Nevertheless, it is

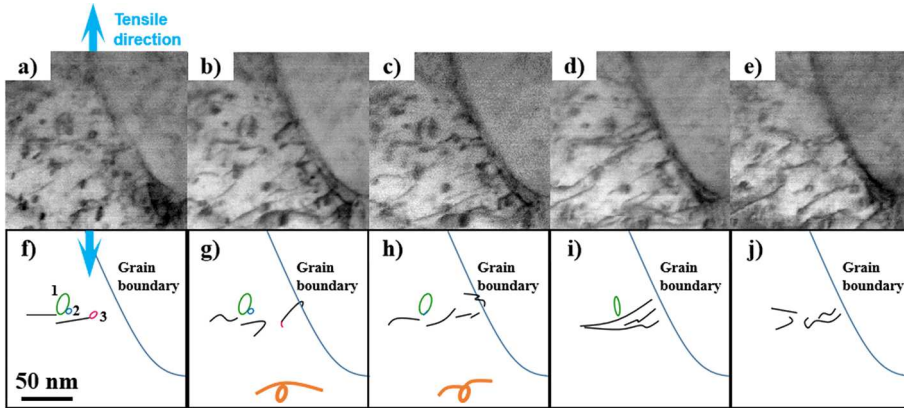


Figure 3. (a-e) Sequential inverted-contrast STEM-HAADF micrographs highlighting the dynamic behaviour of three marked dislocation loops under tensile straining. (f-j) The corresponding simplified schematics depict the evolution of the three marked dislocation loops. The ‘gull-wing’ configuration (highlighted in orange in g and h) suggests that line dislocation motion is obstructed by the presence of a pre-existing dislocation loop.

conceivable that neighbouring dislocation activities may contribute to the alteration in the local stress/strain field (as seen in Figure 3f–h), which may potentially facilitate the loop absorption process. Additionally, as the straining persists, the larger loop 1 seems to undergo shrinkage/rotation (Figure 3i) and eventually disappear due to neighbouring dislocation activities. Upon comparing Figure 3a, e, fewer loops and more line dislocations are evident in the latter than in the former. Interestingly, the line dislocations in the lower regions of Figure 3b, g appear to align with the tensile direction, with anchor points forming characteristic dipole configurations, often referred to as ‘gull-wing’ shapes (Figure 3c, h). This observation confirms that dislocation loops can serve as obstacles, impeding the movement of line dislocations.

As the straining continued, the frequency of line dislocation-loop interactions increased significantly. This first resulted in the formation of dislocation networks (irregular configurations involving line dislocations and loops) and, finally, loops being absorbed by the connected line dislocations. These mechanisms are illustrated in the sequential inverted-contrast STEM-HAADF micrographs in Figure 4. For instance, in Figure 4b, the marked loop 1 is intercepted by a gliding line dislocation from the top-right. First, this interaction distorted the marked loop 1 (Figure 4c) and later formed a complex irregular configuration with the line dislocation and adjacent loop 2 (Figure 4d). In another instance, in the marked loop-line dislocation configuration in Figure 4e, the loop appears to have shrunk upon straining (Figure 4f). This suggests that the part of the loop is consumed by the connected line dislocation, which is confirmed by the fact that the whole loop is finally absorbed by the line dislocation in Figure 4g. Line dislocation-defect interaction, including absorption of dislocation loop by line dislocations, was a subject of extensive molecular dynamic (MD) simulation studies carried out in the past [30–32]. Considering the complexity of the microstructure, these dynamic processes are expected to be aided by the local alterations in the stress/strain fields due to the nearby dislocation activities. Nevertheless, it is essential to note that not all MD

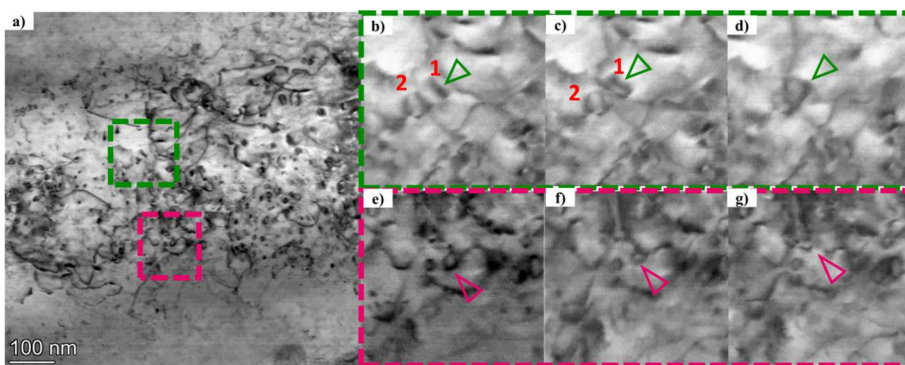


Figure 4. (a) Green and pink dashed frames outline two distinct regions. (b-d) Sequential inverted-contrast STEM-HAADF micrographs under applied strain showcase the dynamic process in which a dislocation loop 1, upon interaction with a mobile line dislocation, is first distorted and later forms a complex irregular configuration with the line dislocation and adjacent loop 2. (e-g) Sequential inverted-contrast STEM-HAADF micrographs under applied strain showcase a marked loop shrinkage in the loop-line dislocation configuration and its complete absorption within the connected line dislocation.

findings can be directly applied to irradiated EUROFER97, given its complex nature, unless future simulation studies establish clear similarities.

The types of dislocation loops and their interactions with line dislocations are also of significant interest. However, due to the double-tilt limitation of the Gatan in-situ straining holder, accurate information regarding the dislocation loop type and habit plane cannot be obtained. As a result, we provide insights based on our previous investigations to address this gap. As mentioned earlier, the quantitative analysis on the irradiated EUROFER97 revealed a higher proportion of larger $\langle 100 \rangle$ type loops than their $\frac{1}{2}\langle 111 \rangle$ smaller counterparts [18,21]. Hence, it is plausible that smaller $\frac{1}{2}\langle 111 \rangle$ loops are more readily absorbed upon interaction with the mobile line dislocations. Whereas the larger $\langle 100 \rangle$ counterparts are less readily absorbed. However, as the straining continues, both $\langle 100 \rangle$ and $\frac{1}{2}\langle 111 \rangle$ type loops will ultimately become a part of the mobile line dislocations. Finally, as the gliding line dislocations annihilate or absorb the loops

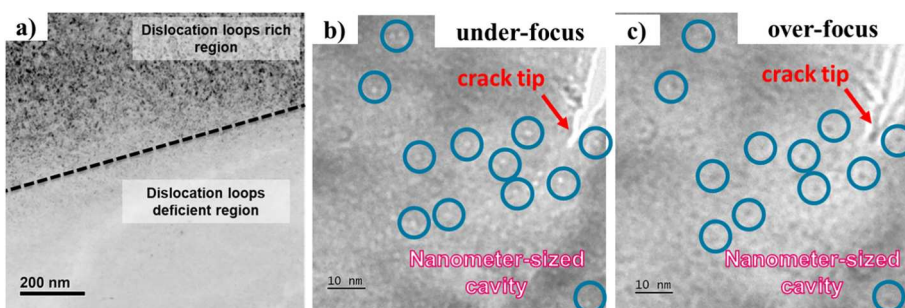


Figure 5. (a) A representative BF-TEM micrograph highlights a dislocation loop-free region formation upon straining. (b, c) Defocused ($\pm 1 \mu\text{m}$) BF-TEM micrographs showcasing the formation of nanometer-sized cavities upon straining.

and deformation becomes localised, a dislocation loop-free zone develops within the middle of the strained lamella (see Figure 5a).

To further advance the understanding of dislocation loop mobility and absorption mechanisms, future studies could utilise double-tilt straining holders or MEMS-based platforms with integrated force measurement. This would help overcome current geometrical limitations and provide more fundamental insights.

Figure 5 and Figure 6 provide insights into crack initiation and propagation phenomena. A notable characteristic of the microstructure during this stage is the appearance of nanometer-sized cavities within the dislocation loop-free zone (refer to Figure 5a–c). The cavities were made discernible by applying the focal series method in BF-TEM imaging mode (as shown in Figure 5b and c). Evidently, the cavities are present in a very high density (around 10^{23} m^{-3}) and appear to be induced by deformation, as they were not distinguishable in stage III, see Figure 2g. The local irradiation-induced clusters or remnants of absorbed dislocation loops or irradiation-induced cavities could be the source of their formation. In contrast to irradiation-induced cavities, the distribution of the deformation-induced cavities is relatively more uniform, and their density is relatively higher.

As depicted in Figure 6a and b, a notable observation is the simultaneous initiation of multiple cracks in the deformation localised region. This is followed by their propagation and eventual coalescence, leading to the final fracture of the FIB lamella. Magnified BF-TEM micrographs acquired near the crack edges unveil the deformation-induced nanometer-sized cavities' pronounced alignment and coalescence (Figure 6c and d). This phenomenon sheds light on the critical role of these nanometer-sized cavities in the

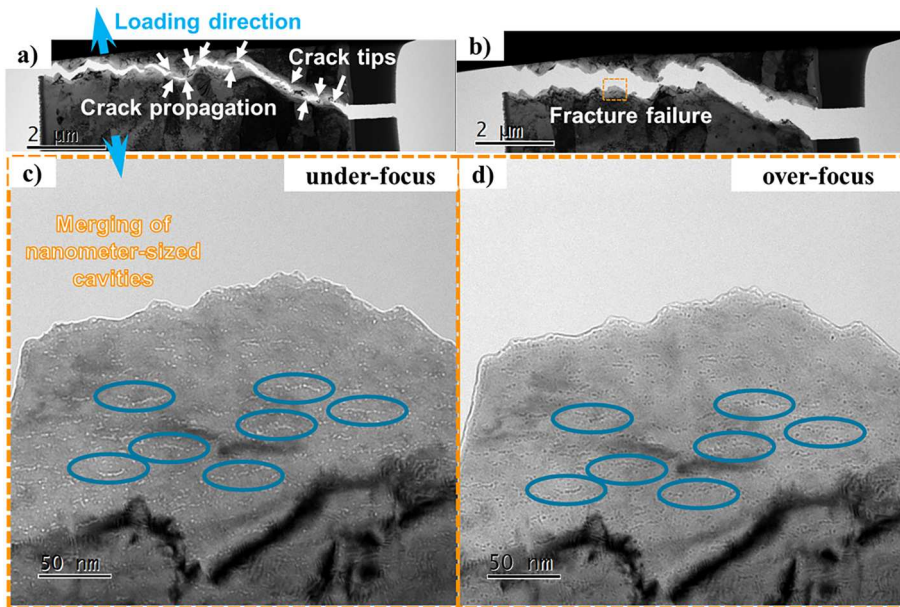


Figure 6. (a) Shows marked cracks formed within deformation-localised zones upon straining. (b) Cracks coalesce, resulting in the final fracture of the lamella. (c, d) Magnified under- and over-focused ($\pm 1 \mu\text{m}$) BF-TEM micrographs from the marked region in (b) exhibit coalescence of nanometer-sized cavities near the cracked edge.

ultimate failure of the irradiated sample. It is noteworthy that distinguishing the contributions of irradiation- and deformation-induced cavities to the final fracture mechanism is challenging due to their similar size (~ 2 nm). However, the density of the deformation-induced cavities (10^{23} m^{-3}) is higher than that of the irradiation-induced cavities (10^{21} m^{-3}), indicating a difference of two orders of magnitude. Therefore, cavities did originate during straining, ultimately contributing to the failure.

4. Summary

In summary, we employed in-situ S/TEM techniques to examine the deformation and damage mechanisms in neutron-irradiated EUROFER97 steel exposed to a 15 dpa dose at 330°C. This work complements the ex-situ TEM characterisation of as-irradiated and post-irradiation deformed microstructure. Analysis of the as-irradiated microstructure revealed a high density of uniformly distributed dislocation loops and a sparse population of non-uniformly distributed nanometer-sized cavities and line dislocations. During in-situ straining experiments on FIB lamella, initial observations indicated the interaction of mobile line dislocations with the loops, resulting in loop absorption and the formation of dislocation networks – an irregular configuration involving line dislocations and loops. Subsequent straining led to a dislocation-loop-free zone, with deformation localising primarily in the lamella's central region. Following this, deformation-induced nanometer-sized cavities emerged within the dislocation-loop-free zone, which likely nucleated at local irradiation-induced clusters/cavities or the remnants of absorbed loops. In contrast to irradiation-induced cavities, the distribution of deformation-induced cavities is relatively more uniform, with a higher density. Concurrently, the alignment and coalescence of nanometer-sized cavities initiated micro-cracks at several locations, which ultimately connected and led to the failure of the lamella. This suggests premature failure of the irradiated sample compared to its unirradiated counterpart, highlighting irradiation-induced embrittlement.

Acknowledgments

The authors would like to thank all the members of the Fusion Materials Laboratory (FML) of the Karlsruhe Institute of Technology (KIT), Germany, for their help in handling irradiated materials. In addition, Ms. Blem and KIT Technik-Haus are acknowledged for fabricating tensile grids. This work has been carried out within the framework of the EUROfusion Consortium, funded by the European Union via the Euratom Research and Training Programme (Grant Agreement No 101052200 – EUROfusion). Views and opinions expressed are however those of the author(s) only and do not necessarily reflect those of the European Union or the European Commission. Neither the European Union nor the European Commission can be held responsible for them.

Disclosure statement

No potential conflict of interest was reported by the author(s).

Funding

This work was supported by EUROfusion: [Grant Number 101052200].

ORCID

Ankur Chauhan  <http://orcid.org/0000-0002-6798-5882>

References

- [1] E. Gaganidze, H.-C. Schneider, B. Dafferner, and J. Aktaa, J. Nucl. Mater. 355 (2006), pp. 83.
- [2] E. Gaganidze, C. Petersen, E. Materna-Morris, C. Dethloff, O.J. Weiss, J. Aktaa, A. Povstyanko, A. Fedoseev, O. Makarov, and V. Prokhorov, J. Nucl. Mater. 417 (2011), pp. 93.
- [3] O.J. Weiss, E. Gaganidze, and J. Aktaa, J. Nucl. Mater. 426 (2012), pp. 52.
- [4] E. Materna-Morris, R. Lindau, H.C. Schneider, and A. Moslang, Fusion Eng. Des. 98-99 (2015), pp. 2038.
- [5] C. Dethloff, E. Gaganidze, and J. Aktaa, J. Nucl. Mater. 454 (2014), pp. 323.
- [6] Z. Jiao, S. Taller, K. Field, G. Yeli, M.P. Moody, and G.S. Was, J. Nucl. Mater. 504 (2018), pp. 122.
- [7] A. Möslang, E. Diegele, M. Klimiankou, R. Lässer, R. Lindau, E. Lucon, E. Materna-Morris, C. Petersen, R. Pippan, and J. Rensman, Nucl. Fusion 45 (2005), pp. 649.
- [8] B. Van der Schaaf, D. Gelles, S. Jitsukawa, A. Kimura, R. Klueh, A. Möslang, and G. Odette, J. Nucl. Mater. 283 (2000), pp. 52.
- [9] U. Stamm, and H. Schroeder, J. Nucl. Mater. 155 (1988), pp. 1059.
- [10] T. Yamamoto, G.R. Odette, H. Kishimoto, J.-W. Rensman, and P. Miao, J. Nucl. Mater. 356 (2006), pp. 27.
- [11] A. Seeger, *Kristallplastizität*, in *Kristallphysik II/Crystal Physics II*, Springer, Berlin, Heidelberg, 1958, p. 1.
- [12] G.S. Was, *Fundamentals of Radiation Materials Science: Metals and Alloys*, Springer, New York, NY, 2016.
- [13] F. Bergner, M. Hernández-Mayoral, C. Heintze, M.J. Konstantinović, L. Malerba, and C. Pareige, Metals-Basel 10 (2020), pp. 147.
- [14] F. Bergner, C. Pareige, M. Hernández-Mayoral, L. Malerba, and C. Heintze, J. Nucl. Mater. 448 (2014), pp. 96.
- [15] F. Onimus, L. Dupuy, and F. Momprou, Prog. Nucl. Energ. 57 (2012), pp. 77.
- [16] J. Drouet, L. Dupuy, F. Onimus, and F. Momprou, Scripta Mater. 119 (2016), pp. 71.
- [17] H.-H. Jin, C. Shin, and J. Kwon, J. Nucl. Mater. 442 (2013), pp. S851.
- [18] A. Chauhan, Q. Yuan, C. Dethloff, E. Gaganidze, and J. Aktaa, J. Nucl. Mater. 548 (2021), pp. 152863.
- [19] Q. Yuan, A. Chauhan, E. Gaganidze, and J. Aktaa, J. Nucl. Mater. 558 (2022), pp. 153366.
- [20] C. Dethloff, E. Gaganidze, and J. Aktaa, Nucl. Mater. Energy 9 (2016), pp. 471.
- [21] C. Dethloff, E. Gaganidze, and J. Aktaa, Nucl. Mater. Energy 15 (2018), pp. 23.
- [22] C. Petersen, J. Aktaa, E. Diegele, E. Gaganidze, R. Lässer, E. Lucon, E. Materna-Morris, A. Möslang, A. Povstyanko, V. Prokhorov, J.W. Rensman, B. van der Schaaf and H.C. Schneider, Mechanical properties of reduced activation ferritic/martensitic steels after European reactor irradiations, 21st IAEA Fusion Energy Conf., Chengdu, People's Republic of China, October 16-21, 2006 Proc.publ.in the web Wien: IAEA, 2006 Paper FT/1-4Ra (Proceedings Series), 2006.
- [23] Q. Yuan, A. Chauhan, E. Gaganidze, and J. Aktaa, J. Nucl. Mater. 558 (2022), pp. 153365.
- [24] T. Groves, Ultramicroscopy 1 (1975), pp. 15.
- [25] Q. Yuan, *Evolution of Irradiation Defects in Fusion Structural Steels at High Temperatures*, KIT Scientific Publishing, Karlsruhe, 2022.
- [26] E. Gaganidze, and J. Aktaa, Fusion Eng. Des. 88 (2013), pp. 118.
- [27] E. Materna-Morris, M. Klimenkov, and A. Möslang, *The Influence of Boron on Structural Properties of Martensitic 8-10% Cr-Steels*, in *Materials Science Forum*, Trans Tech Publ, 2013, pp. 877.
- [28] N. Hashimoto, R. Klueh, M. Ando, H. Tanigawa, T. Sawai, and K. Shiba, Fusion Sci. Technol. 44 (2003), pp. 490.

- [29] H. Tanigawa, R.L. Klueh, N. Hashimoto, and M.A. Sokolov, *J. Nucl. Mater.* 386 (2009), pp. 231.
- [30] Y.N. Osetsky, Y. Matsukawa, R. Stoller, and S. Zinkle, *Phil. Mag. Lett.* 86 (2006), pp. 511.
- [31] Z. Wang, M. Yu, X. Long, C. Yang, N. Gao, Z. Yao, and X. Wang, *Results Phys.* 34 (2022), pp. 105226.
- [32] D. Terentyev, P. Grammatikopoulos, D.J. Bacon, and Y.N. Osetsky, *Acta Mater.* 56 (2008), pp. 5034.
- [33] R. Chaouadi, . *J. Nucl. Mater.* 372 (2008), pp. 379–390. doi:[10.1016/j.jnucmat.2007.04.044](https://doi.org/10.1016/j.jnucmat.2007.04.044).
- [34] K. Wang, Y. Dai, and P. Spätig, . *J. Nucl. Mater.* 468 (2016), pp. 246–254. doi:[10.1016/j.jnucmat.2015.09.031](https://doi.org/10.1016/j.jnucmat.2015.09.031).
- [35] E. Gaganidze, and C. Petersen, *Post Irradiation Examination of RAFM Steels After Fast Reactor Irradiation up to 71 dpa and < 340°C (ARBOR 2): RAFM Steels: Metallurgical and Mechanical Characterisation*, KIT Scientific Publishing, Karlsruhe, 2011. doi:[10.5445/KSP/1000023594](https://doi.org/10.5445/KSP/1000023594).